LA-7578

C.3

Multiphase Interpenetration of Shocked Materials

LOS ALAMOS SCIENTIFIC LABORATORY
Post Office Box 1663 Los Alamos, New Mexico 87545

Work supported by the US Department of Energy,
Division of Military Applications.

UNITED STATES
DEPARTMENT OF ENERGY
CONTRACT W-7405-ENG. 36

LA-7578
UC-34
Issued: February 1979

Multiphase Interpenetration of Shocked Materials

Thomas L. Cook
Ruth B. Demuth
Francis H. Harlow

MULTIPHASE INTERPENETRATION OF SHOCKED MATERIALS

by

Thomas L. Cook, Ruth B. Demuth, and Francis H. Harlow

ABSTRACT

The Particle-in-Cell method for the numerical solution of problems in fluid dynamics has been extended to the study of shock and rarefaction flows in a multiphase mixture. To test the numerical procedure, we have examined the propagation of sound signals through a mixture in which the theoretical speed is appreciably less than that of either material separately, with results that validate the calculational technique. We also have studied the stability of an interface between a gas and a fragmented metal impacted by a shock or rarefaction. The resulting calculations give an accurate differentiation between the stable case, for which the interface should stay sharp, and the unstable case, for which there should be interpenetration. We present information on both the details of interpenetration and its effects on the overall dynamics.

I. INTRODUCTION

Under several possible circumstances the passage of a shock across a density discontinuity can result in an instability of the interface followed by an interpenetration between the phases. One class of problems occurs when both materials are in a liquid or a vapor phase and the interface between them has had some perturbation impressed upon it. Another class occurs when one material is a liquid or a gas, and the other is a fragmented solid. In either case, instability and penetration take place only when the shock moves from the less dense to the more dense material. When both materials are in a liquid or vapor state, the process is closely related to the classical Rayleigh-Taylor instability of incompressible fluids.

When a shock passes through a liquid or a gas and impinges on a fragmented solid, the detailed dynamics are more complicated. The response of the solid

depends on the extent of interpenetration by the driving gas at the contact surface. The interpenetration can be understood qualitatively in terms of the relative acceleration of material elements near the material interface as the shock first passes over. We illustrate this concept in Fig. 1. In Fig. 1a the shock is incident on the material interface from the low-density gas on the right. In Fig. 1b the acceleration of the fluid elements is shown after the passage of the shock. The lighter fluid elements have less inertia and consequently are accelerated more easily by the impulse. Under certain conditions, which we discuss quantitatively below, interpenetration results. The reverse situation is presented in Figs. 1c and d. The shock is incident from the left through the high-density material and the accelerations are in the opposite direction from those in Fig. 1b. The lighter fluid elements accelerate away from the heavier elements, no interpenetration occurs, and the contact surface remains sharply defined.

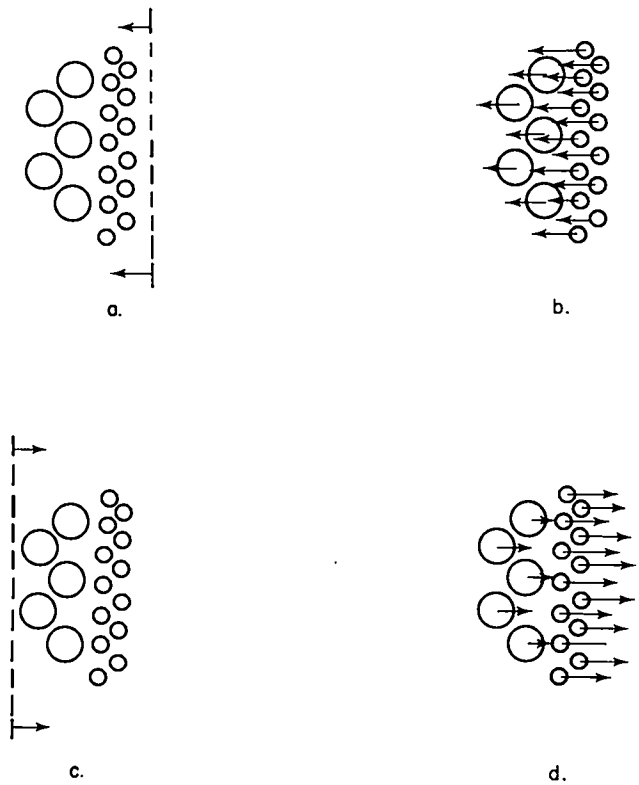

Fig. 1. Relative acceleration of material elements as a shock first passes over.

We examine the effects of shock passage across both forward and trailing edges of a fragmented metallic plate bounded on both sides by a gas of lighter density. This study has required the development of a numerical technique to solve the compressible flow dynamics of two interpenetrating material phases. The first stage of this development used an explicit extension to high speed flows of Eulerian procedures, described in previous publications.[1] The numerical diffusion introduced by the purely Eulerian procedures obscures the finer details of the interface dynamics, especially at the interface where the shock emerges from the fragmented metal and moves into the gas. To improve the accuracy of our solutions (See Appendix A) we have formulated a more elaborate

numerical scheme, based on the Particle-in-Cell (PIC) method.[2] This methodology is implemented in a computer code called PICM.

We describe the newly developed numerical methodology in detail, show its validity in circumstances that admit to analytical solution, address problems that can only be solved numerically, and propose experiments to test these results. Analytical solutions for material mixtures in which the sound speed is less than that in either material are compared to numerical solutions for a two-phase system. To extend this method to more complicated problems, consider the sequence of events described in Fig. 2. In Fig. 2a an infinite-strength shock is incident on the metal from the right. In Fig. 2b the transmitted shock has passed the right contact surface, a reflected shock moves to the right, the gas penetrates the right contact surface, and the metal begins to undergo compression. In Fig. 2c the shock is transmitted into the gas region to the left of the fragmented metal, a rarefaction fan is generated at the left contact surface, and more compaction and interpenetration are evident. The calculation continues until the shock has impacted with the rigid wall. In Fig. 2d the metal rebounds from the rigid wall, gas penetrates the left contact surface, and the right contact surface begins to sharpen as gas is expelled from the mixed region by the rebound shock moving to the right.

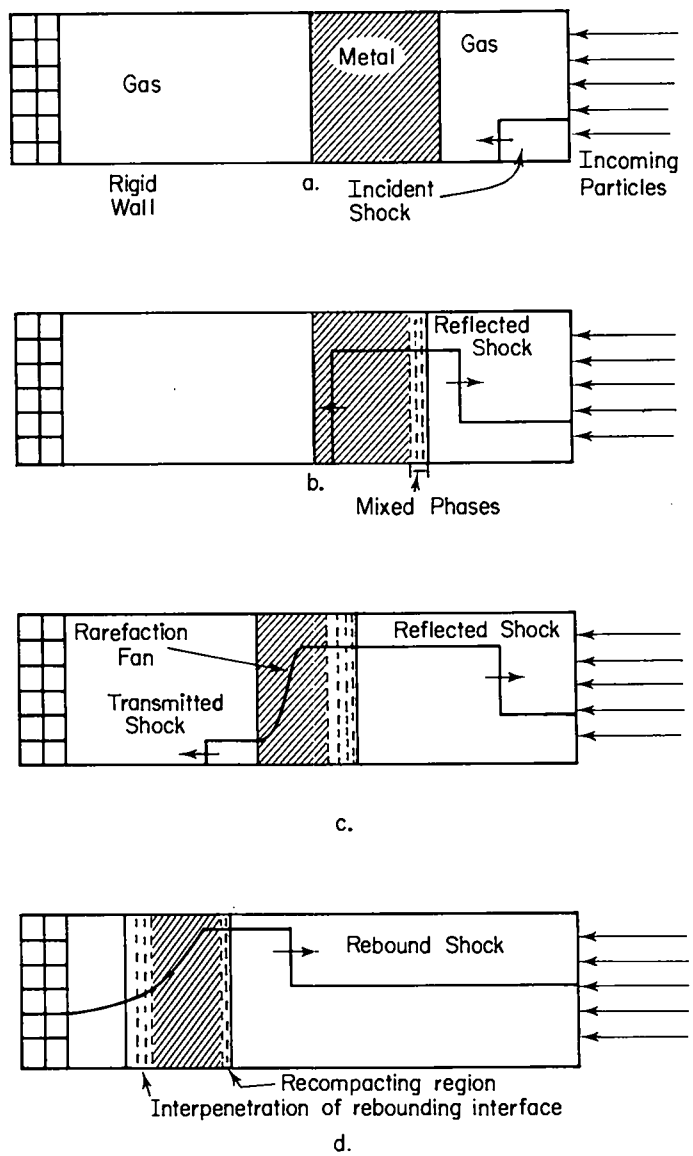

Fig. 2. Shock interaction with a fragmented metal.

II. THE DIFFERENTIAL EQUATIONS

The coupled differential equations and the exchange functions that describe the motion of a fluid composed of many materials, any one of which may be microscopically compressible or incompressible, are discussed in Ref. 3. We summarize below the one-dimensional, two-material, plane coordinate version of these equations.

Mass:

$$\frac{\partial \rho_\ell'}{\partial t} + \frac{\partial \rho_\ell' u_\ell}{\partial x} = 0 \quad , \tag{1}$$

where t is the time; x is the coordinate; ρ_ℓ' is the macroscopic density of material ℓ, that is, the total mass of ℓ per unit total volume, and u_ℓ is the velocity of ℓ.

Momentum:

$$\rho_\ell' \frac{\partial u_\ell}{\partial t} + \rho_\ell' u_\ell \frac{\partial u_\ell}{\partial x} = - \theta_\ell \frac{\partial p}{\partial x} + V_\ell + K_{\ell m} (u_m - u_\ell) \quad . \tag{2}$$

The volume fraction of ℓ is θ_ℓ, the change in momentum of ℓ from the action of artificial viscous forces is V_ℓ, the drag function resulting from motion relative to material m is $K_{\ell m}$, and the pressure is p. It is postulated that the two materials are in local equilibrium, so we do not subscript p. We represent V_ℓ by

$$V_\ell = - \frac{\partial q_\ell}{\partial x} \quad , \tag{3}$$

where q_ℓ is the artificial viscous stress. This stress is calculated by

$$q_\ell = - \rho_\ell' \nu_\ell \frac{\partial u_\ell}{\partial x} \quad , \tag{4}$$

where ν_ℓ is the kinematic viscosity of ℓ. The drag function,[4] which controls the exchange of momentum between the materials, can be written in a simplified form for the case in which ℓ is the dispersed phase (the fragmented metal) and m is the continuous phase (the gas).

$$K_{\ell m} = \frac{3}{8} \frac{C_D}{r_\ell} \theta_\ell \rho_m' |u_\ell - u_m| \quad , \tag{5}$$

where C_D is the drag coefficient and r_ℓ is the radius of a particle of ℓ. Energy:

$$\rho_\ell' \frac{\partial I_\ell}{\partial t} + \rho_\ell' u_\ell \frac{\partial I_\ell}{\partial x} = (\theta_\ell p + q_\ell) \frac{1}{\rho_\ell} \frac{d\rho_\ell}{dt} + \rho_\ell' K_{\ell m} \frac{(u_m - u_\ell)^2}{\rho_\ell' + \rho_m'}$$

$$+ \frac{\partial}{\partial x} \cdot \left(\rho_\ell' \xi_\ell \frac{\partial I_\ell}{\partial x} \right) \quad , \tag{6}$$

where I_ℓ is the specific internal energy and ξ_ℓ is the thermal conductivity. The equation of state of the materials completes the set. For this study we use the stiffened gas formulation,

$$p = a_\ell^2(\rho_\ell - \rho_{0\ell}) + (\gamma_\ell - 1)\rho_\ell I_\ell \quad . \tag{7}$$

The microscopic density, ρ_ℓ, is the mass of ℓ per unit volume occupied by ℓ, so that $\rho_\ell' = \theta_\ell \rho_\ell$. The parameters a_ℓ, $\rho_{0\ell}$, and γ_ℓ characterize the material.

III. NUMERICAL METHODOLOGY

The basic procedure used in the PIC method can be qualitatively described in the following way. The spatial domain of interest is subdivided into a set of Eulerian computational cells. With each cell we associate such field variables as pressure, specific internal energy, and fluid velocity. In addition, we superimpose a Lagrangian set of marker particles. Each particle represents an element of fluid that moves through the Eulerian mesh and interacts with other elements of fluid in a procedure that couples the two materials together. The passage of time is divided into a sequence of computational cycles, each with duration δt. After specification of initial and boundary conditions the evolution of the configuration through time is accomplished by a prescribed set of calculational phases in each cycle. These phases can be summarized as follows.

Phase 1. An advancement of the field variables for each Eulerian cell is calculated as if both the particles and the cells follow the fluid motion. In this phase, therefore, no convective terms in the equations are calculated.

Phase 2. With the Eulerian cells returned to their original positions, the new particle coordinates are calculated and any resulting transport of a particle from one Eulerian cell to another is accompanied by calculations of the corresponding convection of mass, momentum, and energy.

Phase 3. The diffusion of heat is calculated.

The Eulerian calculational mesh and indexing scheme for a typical problem are shown in Fig. 3. Eulerian cell centers are identified by integers, interfaces by half-integers. The index $\bar{j}$ is the total number of interior cells. The indices j_1 and j_2 define regional interfaces. The three interior regions are initialized to contain either of two materials or mixtures thereof. The left boundary is a rigid wall. At the right boundary we allow particles to be fluxed into the system from the exterior boundary cell according to prescribed conditions.

The Lagrangian particles are superimposed on this Eulerian mesh, their coordinates being denoted by the variable $x_{\ell k}$. The first subscript denotes the material; for this particular study, ℓ is either 1 or 2. The second subscript identifies the particle. The initial number of particles of ℓ in a cell is N_ℓ. The total number of particles of ℓ that are interior to the mesh is $N_{\ell I}$, whereas the total number of particles of ℓ, including the particles held in reserve in the exterior boundary region, is $N_{\ell T}$.

As the system evolves through time, the Lagrangian particle distribution changes within the cells throughout the Eulerian mesh, determining the

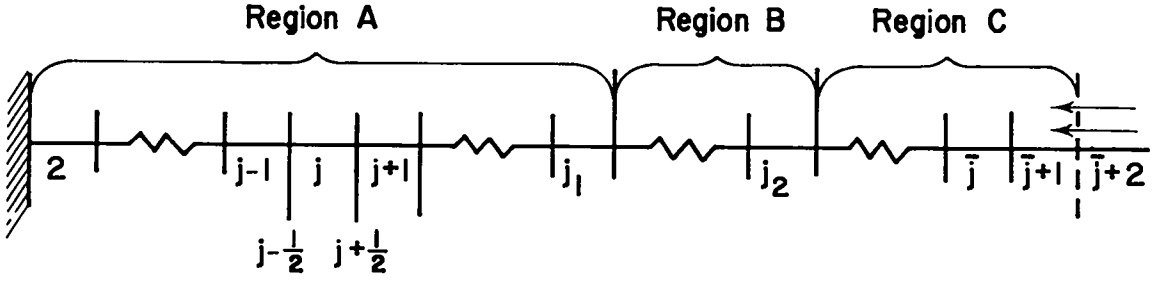

Fig. 3. The Eulerian calculation mesh for a typical problem.

corresponding variations in the macroscopic fluid properties. The centering of the field variables is illustrated in Fig. 4. A complete set of variables must be specified for each material present. The first subscript identifies the material; the second subscript indicates the centering of the variable. For two variables this categorization scheme is simplified. Since we assume pressure equilibrium between the materials, we drop the leading subscript for this variable and indicate only its location in the calculational mesh. The coupling coefficient K for a two-material system is likewise completely specified by indicating location. Pressure (p_j), volume fraction ($\theta_{\ell j}$), specific internal energy ($I_{\ell j}$), macroscopic and microscopic densities ($\rho'_{\ell j}$ and $\rho_{\ell j}$, where $\rho'_{\ell j} = \theta_{\ell j}\rho_{\ell j}$), total mass ($M_{\ell j}$), total internal energy ($E_{\ell j}$), cell volume ($V_{\ell j}$), and artificial viscous pressure ($q_{\ell j}$) are cell-centered quantities. Fluid velocity ($u_{\ell j+\frac{1}{2}}$), coupling coefficient between the fields ($K_{j+\frac{1}{2}}$), edge mass ($\overline{M}_{\ell j+\frac{1}{2}}$), and momentum ($Y_{\ell j+\frac{1}{2}}$) are interface variables. Such cell-wise total quantities as mass M and volume V, are actually per unit cross-sectional area of the one-dimensional system. Previous calculations with the PIC method have treated the components of fluid velocity as cell-centered quantities. In anticipation of the development of an implicit version (see Appendix B) we have used cell-edge velocities in the present code.

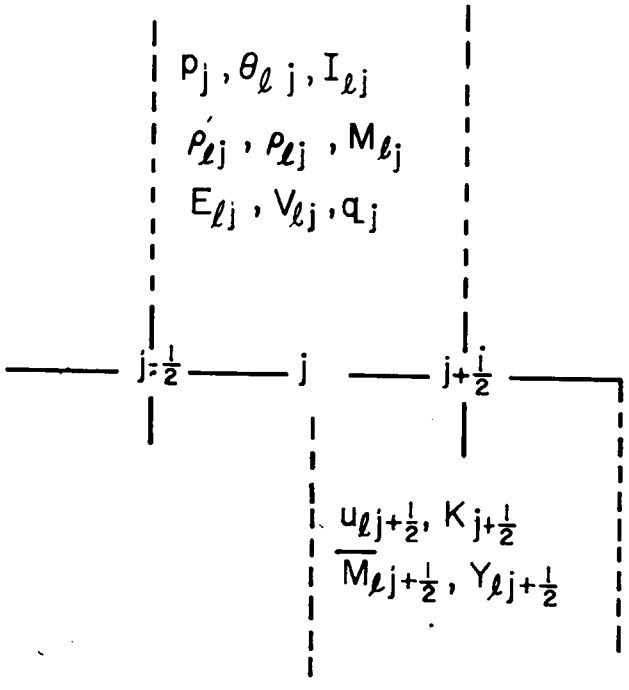

Fig. 4. Centering of the field variables.

In specifying initial conditions we choose the macroscopic fluid variables so that they represent the problem of interest. Consider the case in which region A is a pure gas, region B is fragmented metal, and region C is the same gas as region A. The right wall serves as an inlet boundary for an infinite-strength shock. We choose the initial densities of the fragmented metal disc and of the gas, which together with the Eulerian zone size, determine the total mass initially in every cell. We also set the pressures and the specific internal energies to their prescribed values everywhere in the interior. To initiate a problem,

we select a rate u_{2R} at which the particles are to be fluxed in through the right boundary. The pressure, density, and specific internal energy in the right boundary cell are then determined by the Rankine-Hugoniot equations.[5]

In addition to initializing the field variables, we must arrange the initial particle distribution in a manner consistent with the prescribed fluid properties. The mass m_ℓ of every particle of a given material, wherever it appears in the system, is the same as the mass of every other particle of that same material. This mass is given by

$$m_\ell = \rho'_\ell \, \delta x / N_\ell \quad , \tag{8}$$

where ρ'_ℓ is the initial density in a region with particle density N_ℓ, and δx is the Eulerian cell dimension. We define an initial particle spacing for each region shown in Fig. 3 by dividing the Eulerian cell dimension by the initial particle density of the appropriate material. The particle coordinates are initialized as follows.

$$\begin{aligned}
x_{2i} &= (i - \tfrac{1}{2})\delta x_{2A} && i = 1, \ldots (j_1 - 1)N_2 \quad , \\
x_{2i} &= (j_2 - j_1)\delta x + (i - \tfrac{1}{2})\delta x_{2A} && i = (j_1 - 1)N_2 + 1, N_{2I} \quad , \\
x_{2i} &= \bar{j}\delta x + (i - N_{2I} - \tfrac{1}{2}) \frac{\rho'_{2C}}{\rho'_{2R}} \delta x_{2A} && i = N_{2I} + 1, \ldots N_{2T} \quad , \\
x_{1k} &= (j_1 - 1)\delta x + (k - \tfrac{1}{2})\delta x_{1B} && k = 1, \ldots N_{1I} \quad ,
\end{aligned}$$

where

$$\begin{aligned}
\delta x_{2A} &= \delta x / N_2 = \delta x_{2C} \quad , \\
\delta x_{1B} &= \delta x / N_1 \quad , \\
N_{1I} &= (j_2 - j_1)N_1 \quad , \\
N_{2I} &= (\bar{j} + j_1 - j_2)N_2 \quad , \\
N_{2T} &= N_{2I} + N_R \quad , \\
N_R &= \frac{|u_{2R}| \, T_f}{\delta x} \frac{\rho'_{2R}}{\rho'_{2C}} N_2 \quad .
\end{aligned} \tag{9}$$

The subscripts i and k are the particle indices; δx_{2A}, δx_{1B}, and δx_{2C} are the regional particle separations; N_R is the number of particles held in reserve for the mesh at the right boundary; T_f is the total projected time over which the particles are to be injected, and ρ'_{2R}/ρ'_{2C} is the ratio of densities behind and in front of the input shock.

The initial conditions are not limited to the circumstances described by the above example; any other set of pure or mixed regions can be created, with whatever degree of inhomogeneity desired.

In phase 1 of the calculations we advance the field variables as if both the particles and the cells follow the fluid motion. Left superscripts count the time cycle. The new cell volumes $\tilde{V}_{\ell j}$ are calculated from the old volume δx by

$$\tilde{V}_{1j} = \delta x - \left({}^{n}u_{1j-\frac{1}{2}} - {}^{n}u_{1j+\frac{1}{2}} \right) \delta t$$

and

$$\tilde{V}_{2j} = \delta x - \left({}^{n}u_{2j-\frac{1}{2}} - {}^{n}u_{2j+\frac{1}{2}} \right) \delta t \quad . \tag{10}$$

The artificial viscous pressure is

$$q_{1j} = - \frac{\nu_1 \, {}^{n}M_{ij}}{(\delta x)^2} \left({}^{n}u_{1j+\frac{1}{2}} - {}^{n}u_{1j-\frac{1}{2}} \right)$$

and

$$q_{2j} = - \frac{\nu_2 \, {}^{n}M_{2j}}{(\delta x)^2} \left({}^{n}u_{2j+\frac{1}{2}} - {}^{n}u_{j2-\frac{1}{2}} \right) \quad . \tag{11}$$

If any q_{1j} is calculated less than zero we set it equal to zero. To obtain new velocities at this stage, we solve the two equations of momentum simultaneously. To simplify the mathematical expressions, we define "bar" velocities by writing

$$\bar{u}_{1j+\frac{1}{2}} = {}^{n}u_{1j+\frac{1}{2}} + \frac{\left({}^{n}\theta_{1j} + {}^{n}\theta_{1j+1}\right)\delta t}{2\,{}^{n}\bar{M}_{1j+\frac{1}{2}}}\left({}^{n}p_{j} - {}^{n}p_{j+1}\right) + \frac{\delta t}{{}^{n}\bar{M}_{1j+\frac{1}{2}}}\left({}^{n}q_{1j} - {}^{n}q_{1j+1}\right),$$

$$\bar{u}_{2j+\frac{1}{2}} = {}^{n}u_{2j+\frac{1}{2}} + \frac{\left({}^{n}\theta_{2j} + {}^{n}\theta_{2j+1}\right)\delta t}{2\,{}^{n}\bar{M}_{2j+\frac{1}{2}}}\left({}^{n}p_{j} - {}^{n}p_{j+1}\right) + \frac{\delta t}{{}^{n}\bar{M}_{2j+\frac{1}{2}}}\left({}^{n}q_{2j} - {}^{n}q_{2j+1}\right). \tag{12}$$

If ${}^{n}\bar{M}_{j+\frac{1}{2}} = 0$, then we set $\bar{u}_{\ell j+\frac{1}{2}} = 0$. We now calculate the drag function according to

$$K_{j+\frac{1}{2}} = \frac{3C_D\,{}^{n}\bar{M}_{2j+\frac{1}{2}}}{16\,r_1\,\delta x}\left({}^{n}\theta_{1j} + {}^{n}\theta_{1j+1}\right)\left|{}^{n}u_{1j+\frac{1}{2}} - {}^{n}u_{2j+\frac{1}{2}}\right| + 10^{-7}. \tag{13}$$

The small artificial addition 10^{-7} to the expression for K is present to prevent the occurrence of indefinites in the solution for the velocities when the edge mass ${}^{n}\bar{M}_{2j+\frac{1}{2}}$ is zero.

We now introduce "tilde" velocities ($\tilde{u}_{\ell 2j+\frac{1}{2}}$), which must be modified in the next phase of the calculational cycle to take particle transport into account. They are therefore not the final updated velocities. These "tilde" velocities are given by the simultaneous solution of the two momentum equations,

$$\tilde{u}_{1j+\frac{1}{2}} = \bar{u}_{1j+\frac{1}{2}} + \frac{K_{j+\frac{1}{2}}\delta x\delta t}{\bar{M}_{1j+\frac{1}{2}}}\left(\tilde{u}_{2j+\frac{1}{2}} - \tilde{u}_{1j+\frac{1}{2}}\right)$$

and

$$\tilde{u}_{2j+\frac{1}{2}} = \bar{u}_{2j+\frac{1}{2}} + \frac{K_{j+\frac{1}{2}}\delta x\delta t}{\bar{M}_{2j+\frac{1}{2}}}\left(\tilde{u}_{1j+\frac{1}{2}} - \tilde{u}_{2j+\frac{1}{2}}\right).$$

The solution of these equations is

$$\tilde{u}_{1j+\frac{1}{2}} = \frac{{}^{n}\bar{M}_{1j+\frac{1}{2}}\,{}^{n}\bar{M}_{2j+\frac{1}{2}}\bar{u}_{1j+\frac{1}{2}} + K_{j+\frac{1}{2}}\delta x\delta t\left({}^{n}\bar{M}_{1j+\frac{1}{2}}\bar{u}_{1j+\frac{1}{2}} + {}^{n}\bar{M}_{2j+\frac{1}{2}}\bar{u}_{2j+\frac{1}{2}}\right)}{{}^{n}\bar{M}_{1j+\frac{1}{2}}\,{}^{n}\bar{M}_{2j+\frac{1}{2}} + K_{j+\frac{1}{2}}\,\delta x\delta t\left({}^{n}\bar{M}_{1j+\frac{1}{2}} + {}^{n}\bar{M}_{2j+\frac{1}{2}}\right)}$$

and

$$\tilde{u}_{2j+\frac{1}{2}} = \frac{{}^{n}\bar{M}_{1j+\frac{1}{2}}\,{}^{n}\bar{M}_{2j+\frac{1}{2}}\bar{u}_{2j+\frac{1}{2}} + K_{j+\frac{1}{2}}\delta x\delta t\left({}^{n}\bar{M}_{1j+\frac{1}{2}}\bar{u}_{1j+\frac{1}{2}} + {}^{n}\bar{M}_{2j+\frac{1}{2}}\bar{u}_{2j+\frac{1}{2}}\right)}{{}^{n}\bar{M}_{1j+\frac{1}{2}}\,{}^{n}\bar{M}_{2j+\frac{1}{2}} + K_{j+\frac{1}{2}}\delta x\delta t\left({}^{n}\bar{M}_{1j+\frac{1}{2}} + {}^{n}\bar{M}_{2j+\frac{1}{2}}\right)} \quad . \tag{14}$$

We perform an iteration to obtain the new locally equilibrated pressures. Using volume conservation and the equations of state, we solve the following three equations to obtain a first guess for equilibrium pressure and volume fractions. With $a_2 = 0$ (no "stiffening" in the gas) we have

$$p_j = a_1^2\left(\frac{\rho'_{1j}}{\theta_{1j}} - \rho_{01}\right) + (\gamma_1 - 1)\frac{\rho'_{1j}}{\theta_{1j}}\tilde{I}_{1j} \quad ,$$

$$p_j = (\gamma_2 - 1)\frac{\rho'_{2j}}{\theta_{2j}}\tilde{I}_{2j} \quad ,$$

and

$$\theta_{1j} + \theta_{2j} = 1 \quad .$$

$\tilde{I}_{1j}$ is an approximation to the new specific internal energy that is subsequently modified to take into account dissipation and conduction. The solution of these equations represents a first guess because the internal energies do not include the compressional work that is associated with the changes in volume calculated in this phase. Substituting $M_{\ell j}/\tilde{V}_{\ell j}$ for $\rho'_{\ell j}$ we write

$${}^{n+1}\theta_{2j} = \frac{\beta - \alpha - \gamma_s + \sqrt{(\beta - \alpha - \gamma_s)^2 + 4\beta\gamma_s}}{2\beta} \quad , \tag{15}$$

where

$$\alpha = \frac{{}^{n}M_{1j}}{\tilde{V}_{1j}} \left[a_1^2 + (\gamma_1 - 1)\tilde{I}_{1j} \right] \quad ,$$

$$\beta = a_1^2 \, \rho_{01} \quad ,$$

$$\gamma_s = \frac{(\gamma_2 - 1) \, {}^{n}M_{2j}}{\tilde{V}_{2j}} \tilde{I}_{2j} \quad .$$

If ${}^{n+1}\theta_{2j}$ is less than zero we set it equal to zero and obtain the following solution.

$${}^{n+1}\theta_{1j} = 1 \tag{16}$$

and

$${}^{n+1}p_j = \alpha - \beta \quad . \tag{17}$$

If ${}^{n+1}\theta_{2j}$ is greater than zero we write instead

$${}^{n+1}\theta_{1j} = 1 - {}^{n+1}\theta_{2j} \tag{18}$$

and

$${}^{n+1}p_j = \frac{\gamma_s}{{}^{n+1}\theta_{2j}} \quad . \tag{19}$$

The new values of $\tilde{I}_{1j}$ and $\tilde{I}_{2j}$ are then calculated from the new pressures and volume fractions

$$\tilde{I}_{1j} = {}^{n}I_{1j} - \frac{\left({}^{n+1}p_j + \dfrac{{}^{n}q_{1j}}{{}^{n+1}\theta_{1j}} \right)}{{}^{n}M_{1j}} \left(\tilde{V}_{1j} \, {}^{n+1}\theta_{1j} - \delta x \, {}^{n}\theta_{1j} \right)$$

and

$$\tilde{I}_{2j} = {}^{n}I_{2j} - \frac{\left({}^{n+1}p_j + \frac{{}^{n}q_{2j}}{{}^{n+1}\theta_{2j}}\right)}{{}^{n}M_{2j}} \left(\tilde{V}_{2j}\,{}^{n+1}\theta_{2j} - \delta x\,{}^{n}\theta_{2j}\right) \quad . \tag{20}$$

If ${}^{n}M_{1j}$ or ${}^{n}M_{2j}$ is zero we set the corresponding $\tilde{I}$ equal to zero. With these values of $\tilde{I}$ we repeat the whole equilibration. By examining a set of trial calculations, we have found that five repetitions produce satisfactory accuracy.

The final calculation in phase 1 is the inclusion of the drag-function dissipation in the specific internal energies. To derive an expression for the dissipation, we rewrite the momentum equations in the form

$${}^{n}\bar{M}_{1j+\frac{1}{2}} (\tilde{u}_{1j+\frac{1}{2}} - \bar{u}_{1j+\frac{1}{2}}) = K_{j+\frac{1}{2}}\delta x\delta t(\tilde{u}_{2j+\frac{1}{2}} - \tilde{u}_{1j+\frac{1}{2}})$$

and

$${}^{n}\bar{M}_{2j+\frac{1}{2}} (\tilde{u}_{2j+\frac{1}{2}} - \bar{u}_{2j+\frac{1}{2}}) = K_{j+\frac{1}{2}}\delta x\delta t(\tilde{u}_{1j+\frac{1}{2}} - \tilde{u}_{2j+\frac{1}{2}}) \quad . \tag{21}$$

Multiplying the first equation by $\frac{1}{2}\,(\tilde{u}_{1j+\frac{1}{2}} + \bar{u}_{1j+\frac{1}{2}})$, the second by $\frac{1}{2}\,(\tilde{u}_{2j+\frac{1}{2}} + \bar{u}_{2j+\frac{1}{2}})$, and adding, we obtain

$$\begin{aligned}
&\frac{1}{2}\,{}^{n}\bar{M}_{1j+\frac{1}{2}} \left(\tilde{u}^2_{1j+\frac{1}{2}} - \bar{u}^2_{1j+\frac{1}{2}}\right) + \frac{1}{2}\,{}^{n}\bar{M}_{2j+\frac{1}{2}} \left(\tilde{u}^2_{2j+\frac{1}{2}} - \bar{u}^2_{2j+\frac{1}{2}}\right) \\
&\qquad = \frac{1}{2}\,K_{j+\frac{1}{2}}\delta x\delta t \Big\{\left(\tilde{u}_{2j+\frac{1}{2}} - \tilde{u}_{j+\frac{1}{2}}\right)\left(\tilde{u}_{1j+\frac{1}{2}} + \bar{u}_{1j+\frac{1}{2}}\right) \\
&\qquad + \left(\tilde{u}_{1j+\frac{1}{2}} - \tilde{u}_{2j+\frac{1}{2}}\right)\left(\tilde{u}_{2j+\frac{1}{2}} + \bar{u}_{2j+\frac{1}{2}}\right)\Big\} \quad .
\end{aligned} \tag{22}$$

The left side of the above expression is the change in kinetic energy that results from a coupling of the two fields.

$$\delta KE_{12} = \frac{1}{2}\, {}^{n}\bar{M}_{1j+\frac{1}{2}} \left(\tilde{u}^2_{1j+\frac{1}{2}} - \bar{u}^2_{1j+\frac{1}{2}} \right) + \frac{1}{2}\, {}^{n}\bar{M}_{2j+\frac{1}{2}} \left(\tilde{u}^2_{2j+\frac{1}{2}} - \bar{u}^2_{2j+\frac{1}{2}} \right) \quad . \tag{23}$$

We write the "bar" velocities in Eq. (22) as "tilde" velocities plus terms of order δt. In expanding and rearranging the expression we neglect terms of order $(\delta t)^2$. The result is

$$\delta KE_{12} = -K_{j+\frac{1}{2}} \delta x \delta t \left(\tilde{u}_{2j+\frac{1}{2}} - \tilde{u}_{1j+\frac{1}{2}} \right)^2 \quad . \tag{24}$$

The change in specific internal energy $\delta I_{j+\frac{1}{2}}$ that results from this dissipation of kinetic energy is

$$\delta I_{j+\frac{1}{2}} = \frac{K_{j+\frac{1}{2}} \delta x \delta t \left(\tilde{u}_{2j+\frac{1}{2}} - \tilde{u}_{1j+\frac{1}{2}} \right)^2}{{}^{n}\bar{M}_{1j+\frac{1}{2}} + {}^{n}\bar{M}_{2j+\frac{1}{2}}} \quad . \tag{25}$$

We modify the "tilde" specific internal energies as follows.

$$\tilde{I}_{1j} = \tilde{I}_{1j} + \delta I_{j+\frac{1}{2}} \quad ,$$

$$\tilde{I}_{2j} = \tilde{I}_{2j} + \delta I_{j+\frac{1}{2}} \quad ,$$

$$\tilde{I}_{1j+1} = \tilde{I}_{1j+1} + \delta I_{j+\frac{1}{2}} \quad ,$$

and

$$\tilde{I}_{2j+1} = \tilde{I}_{2j+1} + \delta I_{j+\frac{1}{2}} \quad . \tag{26}$$

In phase 2 we calculate the convective contributions to the equations. We begin by calculating the total momentum in the edge zones and the total internal energy in the cell-centered zones.

$${}^{n}Y_{1j+\frac{1}{2}} = {}^{n}\bar{M}_{1j+\frac{1}{2}}\, \tilde{u}_{1j+\frac{1}{2}} \quad ,$$

$${}^{n}Y_{2j+\frac{1}{2}} = {}^{n}\bar{M}_{2j+\frac{1}{2}}\, \tilde{u}_{2j+\frac{1}{2}} \quad ,$$

$${}^{n}E_{1j} = M_{1j}\, \tilde{I}_{1j} \quad ,$$

and

$$ {}^{n}E_{2j} = M_{2j}\ \tilde{I}_{2j} \quad . \tag{27} $$

To move the particles we first must locate them in the Eulerian mesh. We define an index ${}^{n}j_c$ that corresponds to the cell in which the particle is located at the end of the previous computational cycle. For material 2 we have

$$ {}^{n}j_c = 2 + \text{Integer}\left(\frac{{}^{n}x_{2i}}{\delta x}\right) . \tag{28} $$

We now determine the location of its Eulerian interfaces.

$$ x_{jR} = ({}^{n}j_c - 1)\delta x $$

and

$$ x_{jL} = x_{jR} - \delta x \quad , \tag{29} $$

where the right interface of ${}^{n}j_c$ is x_{jR} and the left interface is x_{jL}. Similarly, we define an integer number that identifies each zone centered on a cell interface.

$$ {}^{n}j_e = \text{Integer}\left(\frac{{}^{n}x_{2i}}{\delta x} + \frac{3}{2}\right) . \tag{30} $$

Using a linear interpolation for the particle velocity we calculate a new location for the particle. To simplify the notation we replace ${}^{n}j_c$ with c and ${}^{n}j_e$ with e.

$$ {}^{n+1}x_{2i} = {}^{n}x_{2i} + \frac{\delta t}{\delta x}\left[\left(x_{jR} - {}^{n}x_{2i}\right)u_{2c-\frac{1}{2}} + \left({}^{n}x_{2i} - x_{jL}\right)u_{2c+\frac{1}{2}}\right] . \tag{31} $$

The quantity ${}^{n+1}x_{2i}$ is the new particle location for the current computational cycle. We must now calculate ${}^{n+1}j_c$ and ${}^{n+1}j_e$ to determine if any cell boundaries have been traversed.

$$^{n+1}j_c = 2 + \text{Integer}\left(\frac{^{n+1}x_{2i}}{\delta x}\right)$$

and

$$^{n+1}j_e = \text{Integer}\left(\frac{^{n+1}x_{2i}}{\delta x} + \frac{3}{2}\right) \quad . \tag{32}$$

To simplify the notation, we replace $^{n+1}j_c$ with d and $^{n+1}j_e$ with f. If $^{n+1}j_c$ does not equal $^{n}j_c$, the particle has crossed from one cell-centered zone to another. Appropriate adjustments must be made in the internal energy and mass of the associated zones. The change in internal energy δE is

$$\delta E = \frac{m_2 \, ^{n}E_{2c}}{^{n}M_{2c}} \quad . \tag{33}$$

The new internal energies are

$$^{n+1}E_{2c} = ^{n}E_{2c} - \delta E$$

and

$$^{n+1}E_{2d} = ^{n}E_{2d} + \delta E \quad . \tag{34}$$

The new mass in each cell is

$$^{n+1}M_{2c} = ^{n}M_{2c} - m_2$$

or

$$^{n+1}M_{2d} = ^{n}M_{2d} + m_2 \quad . \tag{35}$$

If $^{n+1}M_{2c}$ is less than some small fraction of m_2, we set $^{n+1}M_{2c}$ equal to zero.

If ${}^{n+1}j_e$ does not equal ${}^{n}j_e$ the particle has crossed an edge zone, so we adjust the momenta and edge masses. In addition, we modify the internal energy of the appropriate cell-centered zones to allow for the resulting dissipation. To treat the change in internal energy correctly we must relate the edge boundary crossed by the particle to the cell-centered zone containing that boundary. We define an index j_n that contains this information. If ${}^{n+1}j_e$ equals ${}^{n}j_e + 1$, set $j_n = {}^{n}j_c + 3/2$. If ${}^{n+1}j_e$ equals ${}^{n}j_e - 1$, set $j_n = {}^{n}j_c - \frac{1}{2}$. We calculate the change in momentum δY_2 using

$$\delta Y_2 = m_2 \tilde{u}_{2e} \quad . \tag{36}$$

The total momentum in the edge cells becomes

$${}^{n+1}Y_{2e} = {}^{n}Y_{2e} - \delta Y_2$$

and

$${}^{n+1}Y_{2f} = {}^{n}Y_{2f} + \delta Y_2 \quad . \tag{37}$$

To derive the dissipation for this process, we refer to the cells in Fig. 5. Consider a particle of material 2 moving to the right from the $(j + \frac{1}{2})$ edge cell to the $(j + 3/2)$ edge cell. The total kinetic energy KE_b of the particle and the $(j + 3/2)$ cell before the particle enters is

$$KE_b = \frac{1}{2} m_2 \tilde{u}^2_{2j+\frac{1}{2}} + \frac{1}{2} \bar{M}_{2j+3/2} \tilde{u}^2_{2j+3/2} \quad . \tag{38}$$

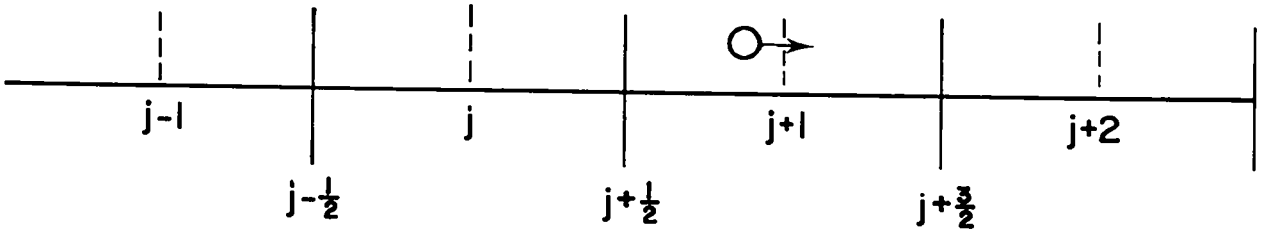

Fig. 5. Particle motion through an Eulerian cell.

The total kinetic energy KE_a of the cell after the particle has entered is

$$KE_a = \frac{1}{2}\left(m_2 + {}^{n}\bar{M}_{2j+3/2}\right){}^{n+1}u^2_{2j+3/2} \quad , \tag{39}$$

where ${}^{n+1}u_{2j+3/2}$ is the new velocity of the (j + 3/2) edge cell. From the conservation of linear momentum we obtain the expression for ${}^{n+1}u_{j+3/2}$. [See Eq. (50).]

$${}^{n+1}u_{2j+3/2} = \frac{m_2\ \tilde{u}_{2j+\frac{1}{2}} + {}^{n}\bar{M}_{2j+3/2}\ \tilde{u}_{2j+3/2}}{m_2 + \bar{M}_{2j+3/2}} \quad . \tag{40}$$

From Eqs. (40) and (39), the new kinetic energy is

$$KE_a = \frac{1}{2}\ \frac{\left(m_2\ \tilde{u}_{2j+\frac{1}{2}} + {}^{n}\bar{M}_{2j+3/2}\ \tilde{u}_{2j+3/2}\right)^2}{m_2 + {}^{n}\bar{M}_{2j+3/2}} \quad . \tag{41}$$

The kinetic energy difference

$$\delta KE = KE_a - KE_b \tag{42}$$

is that amount of energy that must be added as a dissipation term in the internal energy equation. Substituting Eqs. (38) and (41) into Eq. (42); simplifying and rearranging, we obtain

$$\delta KE = -\frac{1}{2}\frac{m_2\ {}^{n}\bar{M}_{2j+3/2}}{m_2 + \bar{M}_{2j+3/2}}\left(\tilde{u}_{2j+3/2} - \tilde{u}_{2j+\frac{1}{2}}\right)^2 \quad . \tag{43}$$

The above expression is negative definite as it must be. We identify j + 3/2 with ${}^{n+1}j_e$ and j + ½ with ${}^{n}j_e$ and accordingly write the dissipation term

$$\delta E_d = \frac{1}{2} \frac{m_2 \, {}^{n}\bar{M}_{2e}}{m_2 + {}^{n}\bar{M}_{2f}} \left(\tilde{u}_{2f} - \tilde{u}_{2e} \right)^2 \quad . \tag{44}$$

We distribute this energy according to the following prescription. If the mass in the neighboring cell is zero we write

$$E_{2c} = E_{2c} + \delta E_d \quad . \tag{45}$$

If, however, the neighboring cell contains mass, we distribute the energy between the two adjacent cell-centered zones. We replace the subscript j_n with g.

$$E_{2c} = E_{2c} + \frac{1}{2} \delta E_d$$

and

$$E_{2g} = E_{2g} + \frac{1}{2} \delta E_d \quad . \tag{46}$$

The edge masses are treated in the same manner as the cell-centered masses. That is,

$${}^{n+1}\bar{M}_{2e} = {}^{n}\bar{M}_{2e} - m_2$$

and

$${}^{n+1}\bar{M}_{2f} = {}^{n}\bar{M}_{2f} + m_2 \quad . \tag{47}$$

If ${}^{n+1}\bar{M}_{2e}$ is less than some small fraction of a particle mass m_2, we set ${}^{n+1}\bar{M}_{2e}$ equal to zero.

The particles of material 1 are moved in analogous fashion, with similar transport of mass, momentum, and energy.

We calculate the new location of each reserve particle by

$${}^{n+1}x_{2i} = {}^{n}x_{2i} + u_{2R} \delta t \quad . \tag{48}$$

If the particle has crossed the mesh boundary, we make the following modifications.

$$N_{2i} = N_{2I} + 1 \quad ,$$

$$E_{2\bar{j}+1} = E_{2\bar{j}+1} + m_2 I_{2R} \quad ,$$

$$^{n+1}M_{2\bar{j}+1} = {}^{n+1}M_{2\bar{j}+1} + m_2 \quad ,$$

and

$$^{n+1}\bar{M}_{2\bar{j}+3/2} = {}^{n+1}\bar{M}_{2\bar{j}+3/2} + m_2 \quad . \tag{49}$$

In the final stage of the phase 2 calculation, we use our newly determined momenta, internal energies, cell-centered masses, and edge masses to obtain updated velocities and specific internal energies. If the edge mass of ℓ is nonzero for a particular zone, we calculate the velocity by

$$^{n+1}u_{\ell j+\frac{1}{2}} = \frac{Y_{\ell j+\frac{1}{2}}}{^{n+1}\bar{M}_{\ell j+\frac{1}{2}}} \quad . \tag{50}$$

If one material is absent from an edge zone, we set the velocity of that material equal to the velocity of the other material.

To obtain the specific internal energies we divide the total internal energy of a cell-centered zone by its total mass.

$$\tilde{I}_{\ell j} = \frac{E_{\ell j}}{^{n+1}M_{\ell j}} \quad . \tag{51}$$

If no mass of ℓ is present in a zone, we set the specific internal energy of that material to zero. At this point the specific internal energies are not final for this computational cycle, so we continue to designate them as "tilde" quantities.

In phase 3 we calculate the contribution of the heat diffusion term to the specific internal energies. We begin by setting the boundary conditions at the rigid wall so that we have no diffusive losses through that boundary.

$$\tilde{I}_{\ell 1} = \tilde{I}_{\ell 2} \quad . \tag{52}$$

The difference form of the second-order partial derivative in the heat diffusion term uses the lesser of the two cell-centered masses adjacent to the interface under consideration, thus avoiding excessive flux to or from a cell with small mass. We refer to these masses as $M_{\ell R}$ and $M_{\ell L}$. The new specific internal energies are given by

$$ {}^{n+1}I_{\ell j} = \tilde{I}_{\ell j} + \frac{\xi \delta t}{{}^{n+1}M_{\ell j}(\delta x)^2}\left[M_{\ell R}\left(\tilde{I}_{\ell j+1} - \tilde{I}_{\ell j}\right) - M_{\ell L}\left(\tilde{I}_{\ell j} - \tilde{I}_{\ell j-1}\right)\right] \quad . \tag{53} $$

If ${}^{n+1}M_{\ell j}$ equals zero we set ${}^{n+1}I_{\ell j}$ equal to zero. With the three phases of the computational cycle complete, we recalculate pressures and volume fractions based on the new specific internal energies.

IV. SOUND SPEED IN A MIXTURE

We have performed two series of studies using the technique introduced above. The first study proof-tests the methodology in circumstances chosen to exhibit the way low sound speed can characterize a two-material mixture. According to the classical theory given by Wood,[6] a low-amplitude signal propagates through a mixture of strongly coupled materials with a speed given by the following equation.

$$ C^2 = \frac{C_1^2 C_2^2 \rho_1 \rho_2}{[\theta_1 C_2^2 \rho_2 + \theta_2 C_1^2 \rho_1][\theta_1 \rho_1 + \theta_2 \rho_2]} \quad , \tag{54} $$

in which C_1 and C_2 are the pure-material sound speeds for the two components of the mixture. We consider first the case in which the ratio of the microscopic densities between the two materials is 11 to 1, with a set of material properties and initial conditions as given in Tables I and II, for which $C_1 = 1.03$ and $C_2 = 1.29$. The mixture sound speed computed by the above equation is $C = 0.74$. To directly proof-test the numerical method for this type of example requires computer calculations for the propagation of a very weak disturbance through the mixture. It has been demonstrated previously however that PIC calculations[7] can develop severe fluctuations when the Mach number of the flow is much smaller than 1. To test the numerical methodology we have performed a series of calculations,

each with a weaker disturbance impressed onto the fluid mixture, and have extrapolated the results for comparison with the low-amplitude limit.

The configuration for the calculations is summarized in Tables II and III and consists of regions A and B, of which A contains the mixture and B the pure gas. In the pure gas we initiate a shock for each calculation, the strength of which is characterized by the Mach number, M, defined as the ratio of the shock speed to the sound speed in the undisturbed gas of region B. In Table IV we indicate the boundary conditions supplied to the right side of the system.

TABLE I

MATERIAL PROPERTIES

ℓ	$\rho_{0\ell}$	γ_ℓ	a_ℓ	C_D	r_1
1	10.0	5/3	1.0	1.0	0.0001
2	0.0	5/3	0.0	-	-

TABLE II

INITIAL CONDITIONS

Region	ρ'_{1j}	ρ'_{2j}	θ_{1j}	θ_{2j}	I_{1j}	I_{2j}	p_j	$u_{1j+\frac{1}{2}}$	$u_{2j+\frac{1}{2}}$
A	8.25	0.25	0.75	0.25	0.0	1.5	1.0	0.0	0.0
B	0.0	1.0	0.0	1.0	0.0	1.5	1.0	0.0	0.0

TABLE III

CALCULATIONAL MESH

Mach No.	DX	DT	j_1	$\bar{j}$	N_1	N_2	ν_1	ν_2	ξ_1	ξ_2
2.0	1.0	0.1	16	30	16	8	0.2	0.2	0.2	0.2
1.5	1.0	0.1	16	30	16	8	0.2	0.2	0.2	0.2
1.1	0.33	0.033	46	90	64	32	0.06	0.06	0.06	0.06

TABLE IV

BOUNDARY CONDITIONS

Mach No.	$\rho'_{1\bar{j}+2}$	$\rho'_{1\bar{j}+2}$	$I_{1\bar{j}+2}$	$I_{2\bar{j}+2}$	$P_{\bar{j}+2}$	$u_{1\bar{j}+3/2}$	$u_{2\bar{j}+3/2}$
2.0	0.0	2.286	0.0	3.117	4.750	0.0	-1.452
1.5	0.0	1.174	0.0	2.242	2.562	0.0	-0.807
1.1	0.0	1.150	0.0	1.647	1.263	0.0	-0.185

In each case we measure the transit time of the signal across A. With M = 2.0, a relatively coarse computational mesh, with 15 cells across the mixture region and with particle densities of 16 and 8 for materials 1 and 2, respectively, produces sufficient resolution of the transmitted signal. We find that the calculation with M = 1.1 requires a finer mesh and higher particle densities to reduce the computational fluctuations associated with the "perturbed stagnation" of the materials, a difficulty that has always required special treatment in PIC based methodologies. This calculation requires 45 cells across the mixture region and particle densities of 64 and 32 per cell for materials 1 and 2, respectively. The calculation with M = 1.5 also has computational fluctuations, albeit to a lesser degree. A plot of the three signal speeds is shown as a function of M in Fig. 6 together with the theoretical result for a weak signal (M = 0). The extrapolated result agrees closely with theory.

As a more stringent test, we have performed a similar set of calculations using a density ratio of 100 to 1. The data for these calculations are given in Tables V-VIII. The pure-material sound speeds of the metal and the gas are C_1 and C_2 = 1, respectively. In this case, the mixture sound speed has the theoretical value C = 0.2, which is 1/5 of the sound speed in either material by itself. Again the extrapolation of the calculated results to M = 0, shown in Fig. 7, agrees closely with theory.

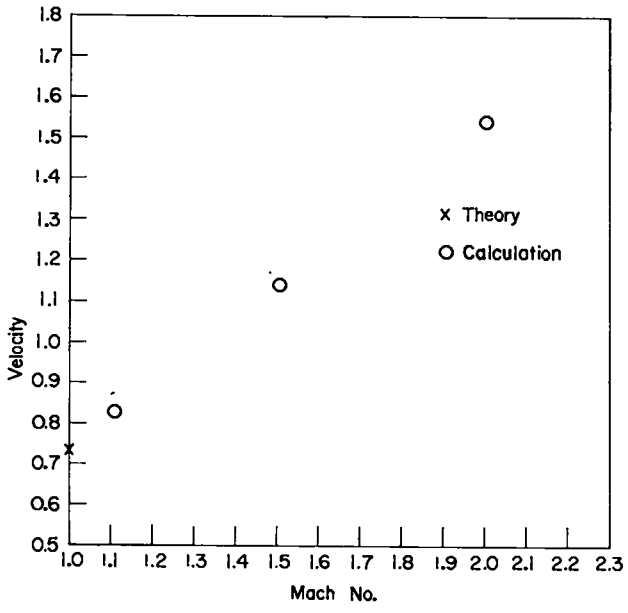

Fig. 6. Signal speed as a function of Mach number.

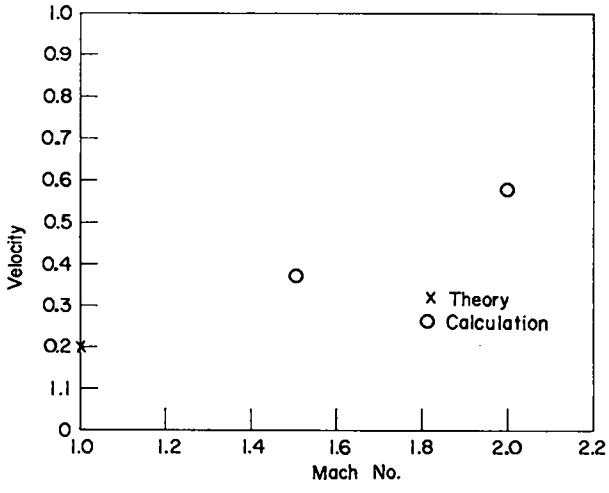

Fig. 7. Signal speed as a function of Mach number.

TABLE V

MATERIAL PROPERTIES

ℓ	$\rho_{0\ell}$	γ_ℓ	a_ℓ	C_D	r_1
1	10.0	5/3	1.0	1.0	0.0001
2	0.0	5/3	0.0	-	-

TABLE VI

INITIAL CONDITIONS

Region	ρ'_{1j}	ρ'_{2j}	θ_{1j}	θ_{2j}	I_{1j}	I_{2j}	p_j	$u_{1j+\frac{1}{2}}$	$u_{2j+\frac{1}{2}}$
A	5.03	0.05	0.5	0.5	0.0	0.9	0.06	0.0	0.0
B	0.0	0.1	0.0	1.0	0.0	0.9	0.06	0.0	0.0

TABLE VII

CALCULATIONAL MESH

Mach No.	DX	DT	j_1	$\bar{j}$	N_1	N_2	ν_1	ν_2	ξ_1	ξ_2
2.0	1.0	0.1	16	30	64	32	0.2	0.2	0.2	0.2
1.5	1.0	0.1	16	30	64	32	0.2	0.2	0.2	0.2

TABLE VIII

BOUNDARY CONDITIONS

Mach No.	$\rho'_{1\bar{j}+2}$	$\rho'_{2\bar{j}+2}$	$I_{1\bar{j}+2}$	$I_{2\bar{j}+2}$	$p_{\bar{j}+2}$	$u_{1\bar{j}+3/2}$	$u_{2\bar{j}+3/2}$
2.0	0.0	0.228	0.0	1.870	0.285	0.0	-1.125
1.5	0.0	0.171	0.0	1.345	0.154	0.0	-0.625

V. FRAGMENTED METALLIC DISC

Having demonstrated the validity of our two-fluid methodology for the examples described above, we proceed to the second set of calculations. In this set we examine the dynamics of a fragmented metal disc impacted by a strong shock. The initial conditions are shown schematically in Fig. 2. As discussed previously, the initial configuration consists of A, a region of pure gas, B, a region of fragmented metal, and C, another region of pure gas. The left wall is idealized as a rigid boundary, whereas the right wall is an inlet boundary through which a shock is introduced. The material properties of the fluids used in the first pair of calculations are summarized in Table I. Tables IX-XI present the initial

conditions, the calculational mesh, and the boundary conditions used in both calculations. The two calculations differ in only one respect; the coupling strength between the gas and the metal fragments is less in the second calculation. The coupling strength is reduced by changing the value of the particle radius r_1 (in Table I) from 0.0001 to 0.01.

TABLE IX

INITIAL CONDITIONS

Region	ρ'_{1j}	ρ'_{2j}	θ_{1j}	θ_{2j}	I_{1j}	I_{2j}	p_j	$u_{1j+\frac{1}{2}}$	$u_{2j+\frac{1}{2}}$
A	0.0	0.1	0.0	1.0	0.0	0.0	0.0	0.0	0.0
B	10.0	0.0	1.0	0.0	0.0	0.0	0.0	0.0	0.0
C	0.0	0.1	0.0	1.0	0.0	0.0	0.0	0.0	0.0

TABLE X

CALCULATIONAL MESH

DX	DT	j_1	j_2	$\bar{j}$	N_1	N_2	ν_1	ν_2	ξ_1	ξ_2
0.1	0.005	201	251	300	20	6	0.15	0.15	0.15	0.15

TABLE XI

BOUNDARY CONDITIONS

$\rho'_{1\bar{j}+2}$	$\rho'_{2\bar{j}+2}$	$I_{1\bar{j}+2}$	$I_{2\bar{j}+2}$	$p_{\bar{j}+2}$	$u_{1\bar{j}+3/2}$	$u_{2\bar{j}+3/2}$
0.0	0.4	0.0	4.5	1.2	0.0	-3.0

Figure 8 presents a summary of the sequence of events as a function of time for the strong-coupling calculation. The world lines are shown for some principal shocks and for the interface motion. Note that even before the metal disc has moved very far toward the rigid wall, the shock in region C has passed back and forth several times between the contact surface and the inlet wall. As a result, the pressure driving the metal disc has been increasing continuously, giving the acceleration shown by the curved world lines of the two interfaces. As the leading surface of the metal disc approaches the wall, the shock that precedes it is reflected back toward the leading edge of the metal and subsequently is reflected many times with increasingly higher frequency between that interface and the wall. The result is a strong deceleration of the metal as the

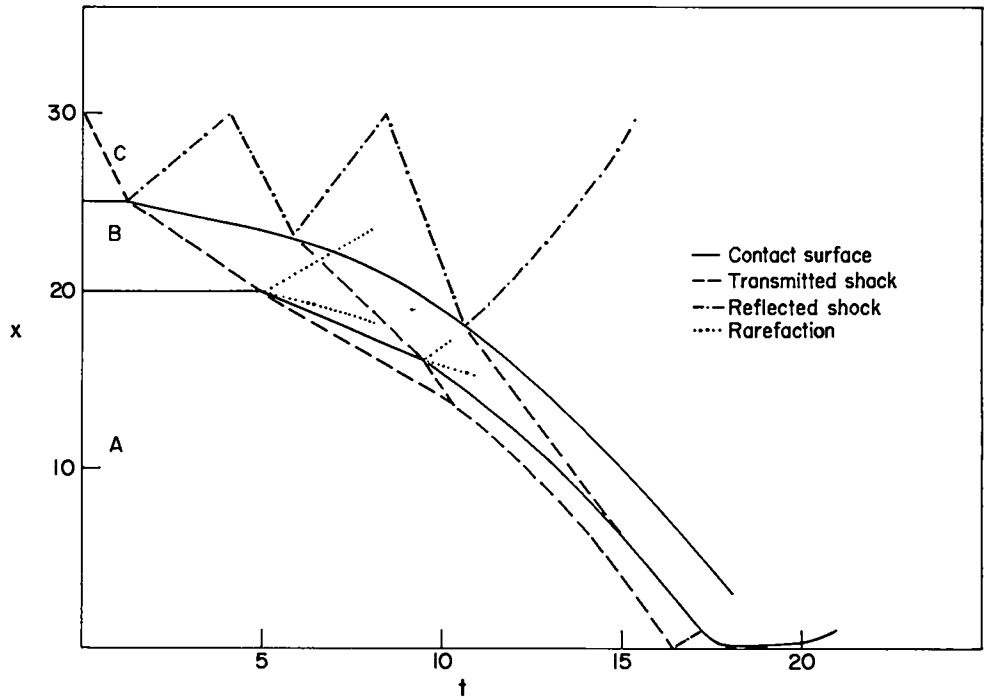

Fig. 8. World lines for the strongly coupled calculation.

gas in region A reaches its maximum compression and then begins to re-expand. In this example with essentially infinite coupling between the two materials, both the leading and trailing contact surfaces remain sharp.

Several stages of the strong-coupling calculation are shown in Figs. 9 and 10. Table XII identifies the labels used in these figures with the symbols defined in preceding sections. At t = 11 the initial shock has traversed the gas in region C through several reflections while the shock transmitted through the metal has reached the gas in region A and has propagated a small distance into that region. The location of the contact surfaces is discerned most clearly in the theta plots of Fig. 10. By comparing the pressure variation at t = 11 to the variation in θ_1 and θ_2, we find that the right-hand contact surface is located at a distance of 17.5, just ahead of the high-pressure spike in region C, which results from the presence of a reflected shock. The

TABLE XII

SYMBOL IDENTIFICATION

P	p
RP1	ρ_1'
RP2	ρ_2'
U1	u_1
U2	u_2
TH1	θ_1
TH2	θ_2
EI1	I_1
EI2	I_2

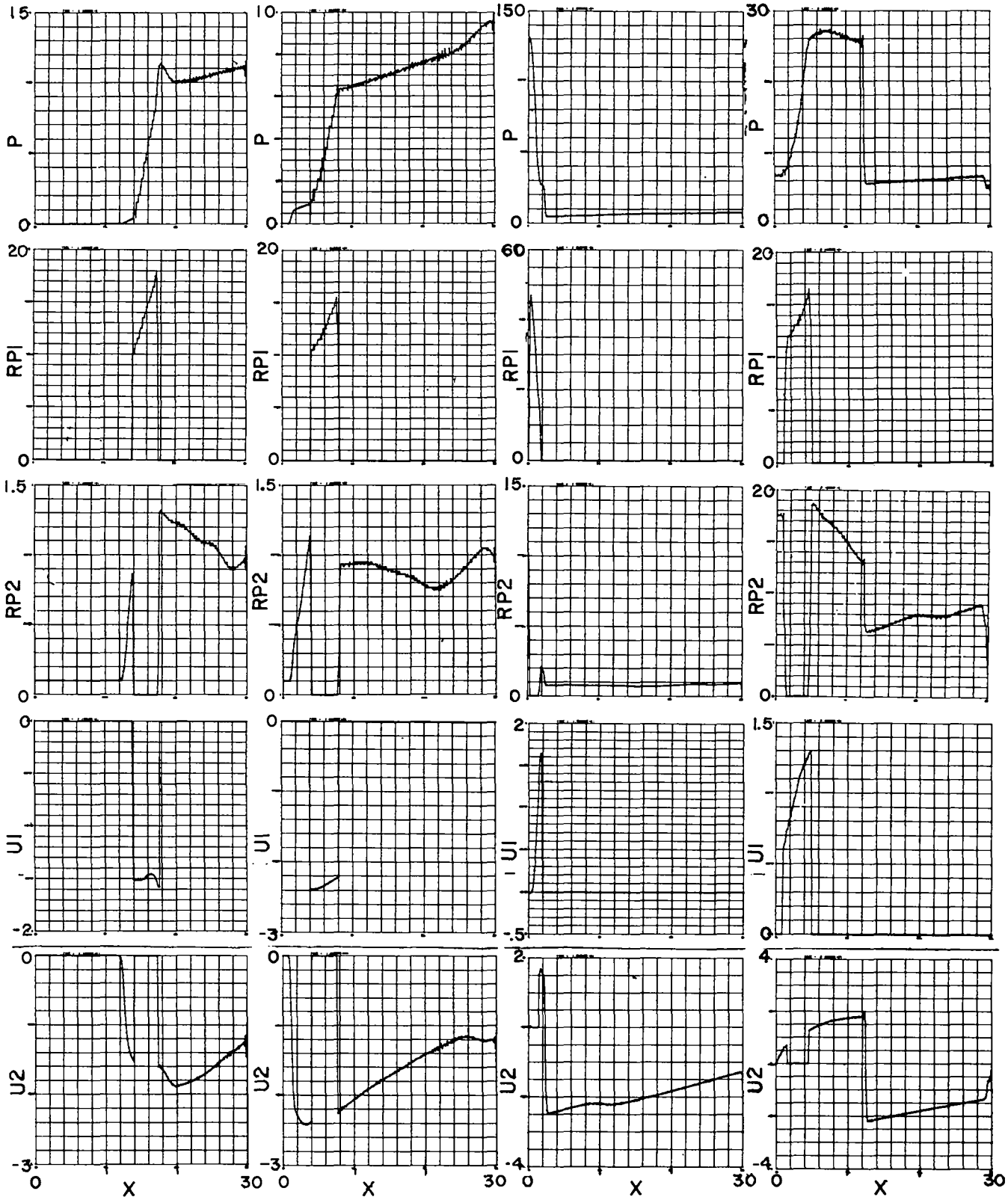

Fig. 9. Field variables as functions of position at times 11, 16, 19, 21; strong coupling between materials.

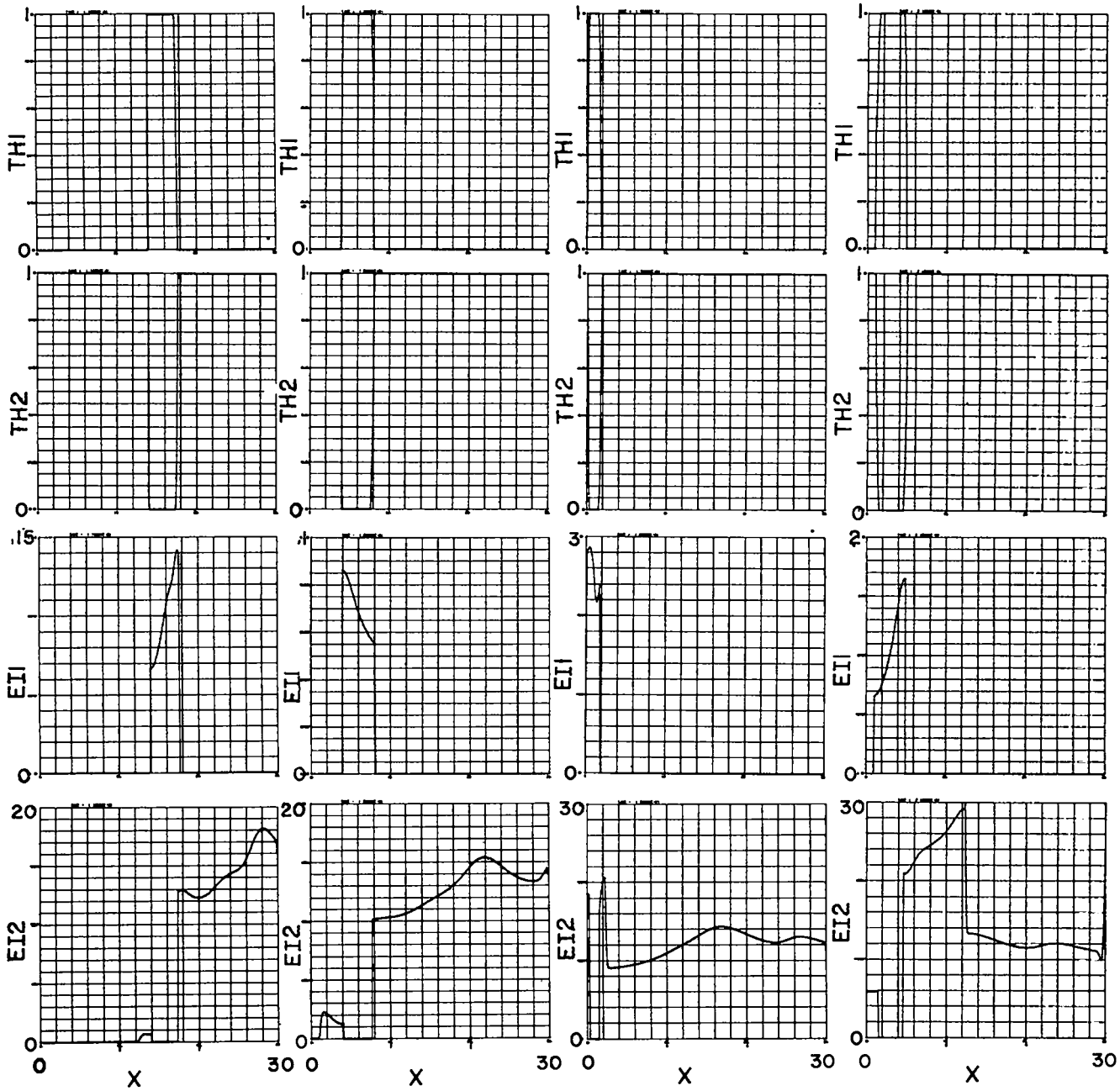

Fig. 10. Field variables as functions of position at times 11, 16, 19, 21; strong coupling between materials.

macroscopic density ρ_2' of the gas adjacent to the metal in region A has increased significantly, as has the specific internal energy I_2. These variables, together with the velocity plot for the gas, indicate that the shock front is located at a distance of 12.5, so that it leads the metallic layer by approximately 1.4. By t = 16, the shock front ahead of the metal is evident in the pressure plots as well as in the plots of ρ_2', I_2, and u_2. From the theta plots we observe that the metal layer is slightly less compacted than it was at t = 11, an effect of the expanding rarefaction fan that eats back into the metal, as shown in the world line plots of Fig. 8.

At t = 19 we show the state of the system just after the turnaround of the metal interface. The maximum macroscopic density in the metal disc has more than quadrupled and the thickness has decreased by more than a factor of 2. Both the metal and the gas have been heated during interaction with the rigid wall. For example, the peak value of the specific internal energy of the fragmented metal has increased by a factor of 33 from its value at t = 16. The velocities in the disc are all positive, indicating that it is rebounding. At t = 21, we see that the metal disc is expanding and continuing to rebound to the right. The strong shock generated by the collision with the rigid wall has now passed well into the gas of region C, heating it and raising its pressure.

The calculation that is to be compared with the one above uses a coupling coefficient that is reduced by two orders of magnitude. We show that with this nominal coupling between the two materials, there is both an interpenetration of the metal fragments by the gas, forming a mix region, and a slight modification to the mean dynamics of both the metal and the gas. Figure 11 shows time sequences of field variables selected for comparison with the strongly coupled results of Figs. 9 and 10. The difference in the dynamical response of the metal disc is indicated by the time evolution of the macroscopic densities. Even at the relatively early time of t = 11, gas interpenetration has lowered the metal densities at the right interface and has reduced the sharpness of that contact surface. There are significant gas densities within the metal itself near the trailing edge of the disc. The leading, stable edge maintains its sharpness until decelerated by the first shock reflected from the rigid wall, at which time it becomes the unstable interface. Shortly afterwards, the right metallic surface becomes stable. The mix region of the right surface recompacts and sharpens as the gas within it is expelled to the right.

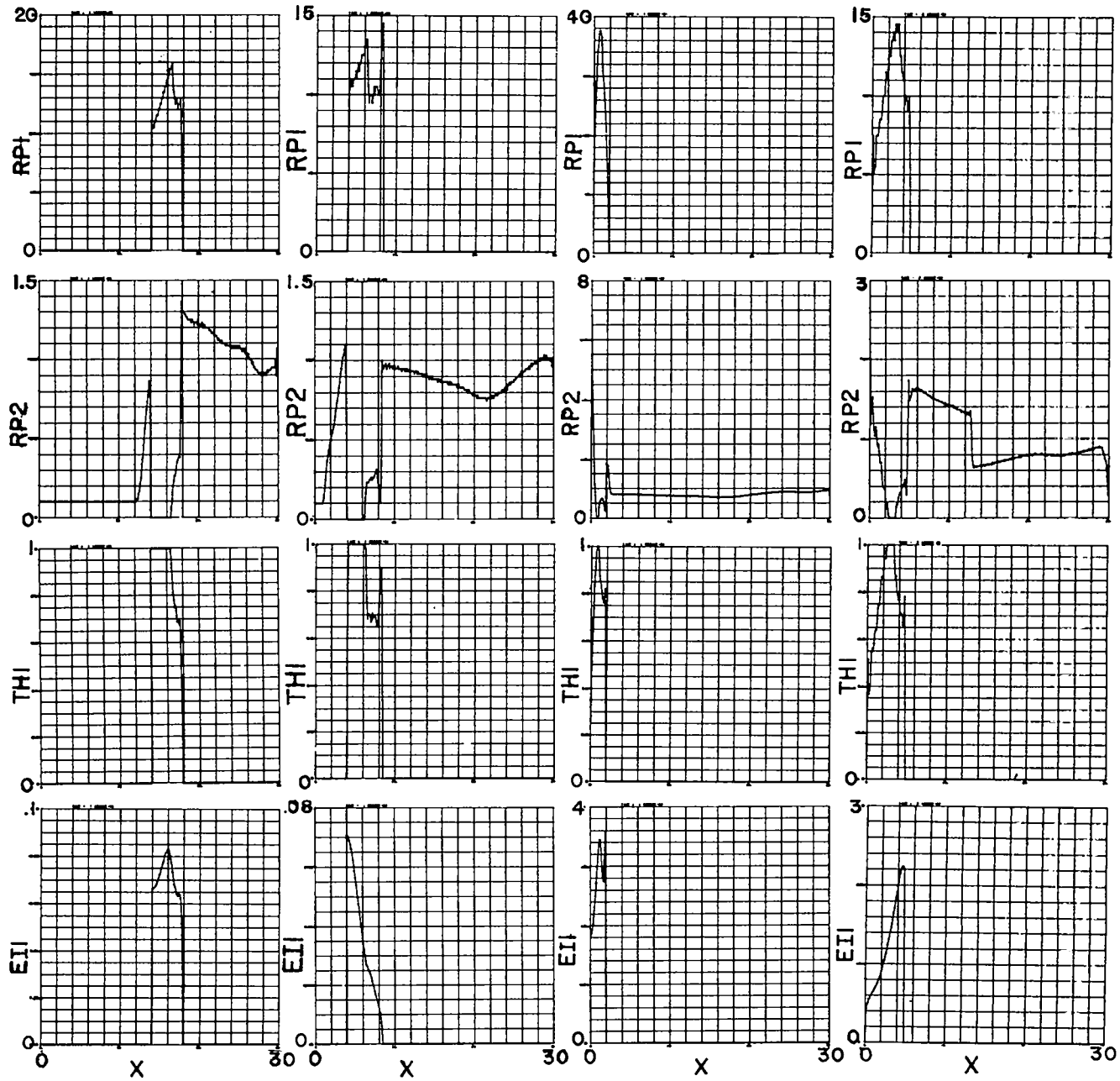

Fig. 11. Field variables as functions of position at times 11, 16, 19, 21; weak coupling between materials.

If we compare the maximum specific internal energy of the metal disc at times before turnaround, we find that the strongly coupled case is the hotter of the two; however, after turnaround the weakly coupled system is the hotter. The macroscopic densities predicted in both cases for the gas of region A are very similar before turnaround. The gross dynamic response of the metal for the weakly coupled case begins to show significant differences from the strongly coupled case after the leading metal interface becomes unstable because of interaction with shocks reflected from the rigid wall. At t = 19 the maximum gas density for the strongly coupled case is 10.5; for the weakly coupled case it is only 6.8. The respective maximum densities in the metal disc are 47.5 and 37.5. Both the compression of the gas in region A and the compaction of the metal disc are greater in the case of strong coupling.

Figure 12 shows the world lines of the disc interfaces for the weakly-coupled case. The shaded areas represent the regions of mix. As discussed above, the left interface is stable until interaction with the shocks reflected from the rigid wall. In the figure this contact surface remains sharp, beginning to smear only after being struck by the first reflected shock. The right interface is unstable before turnaround. This region broadens steadily until turnaround, after which the gas is partially expelled as the now stable interface sharpens. In Fig. 13 the interface world lines are overlayed on an expanded scale. This figure shows that the left contact surface is first stable and then unstable and that the right contact surface is first unstable and then stable.

In Fig. 14 we plot the average microscopic compression of the gas initially in region A for the two calculations. The maximum average compression is higher in the case of the strong coupling. The magnitude of the total momentum in the metal disc is greater for this case, producing higher levels of compression before turnaround. The resulting rebound is more energetic because of the higher pressure that has built up between the rigid wall and the disc, as can be seen from the plot of the total momentum in the metal disc as a function of time in Fig. 15.

Calculations in which the density ratio of the two materials is large are potentially difficult to carry out in multiphase flow studies. The reason for this problem is that a computational cell with a very small amount of mass of the lighter material adjacent to a computational cell with mass of the heavier material can experience very large accelerations. To extend the present calculations to higher density ratios, this difficulty has been remedied by a special

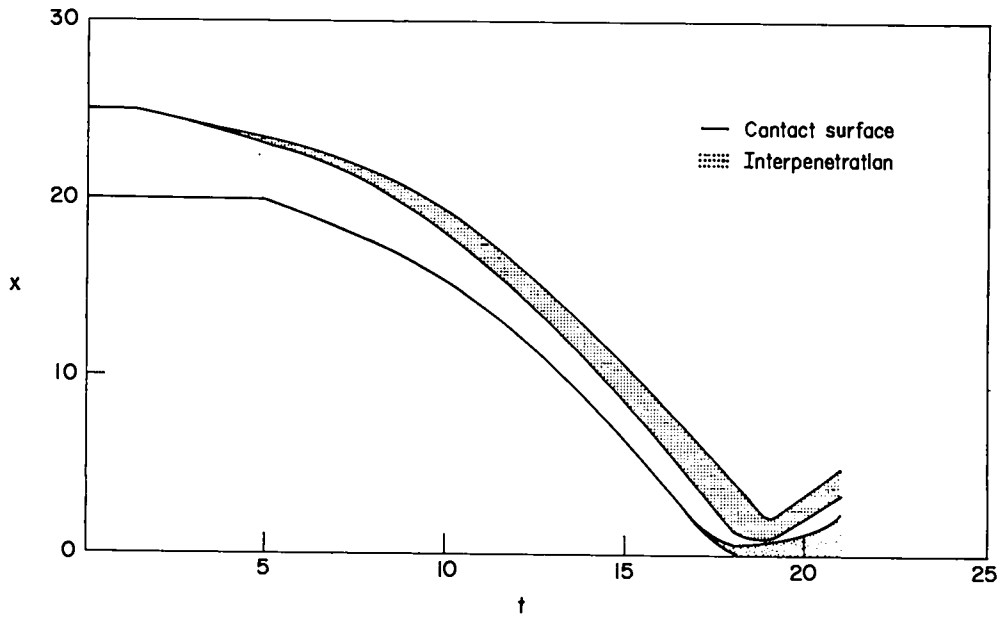

Fig. 12. World lines of the disc interfaces for the nominal coupling case.

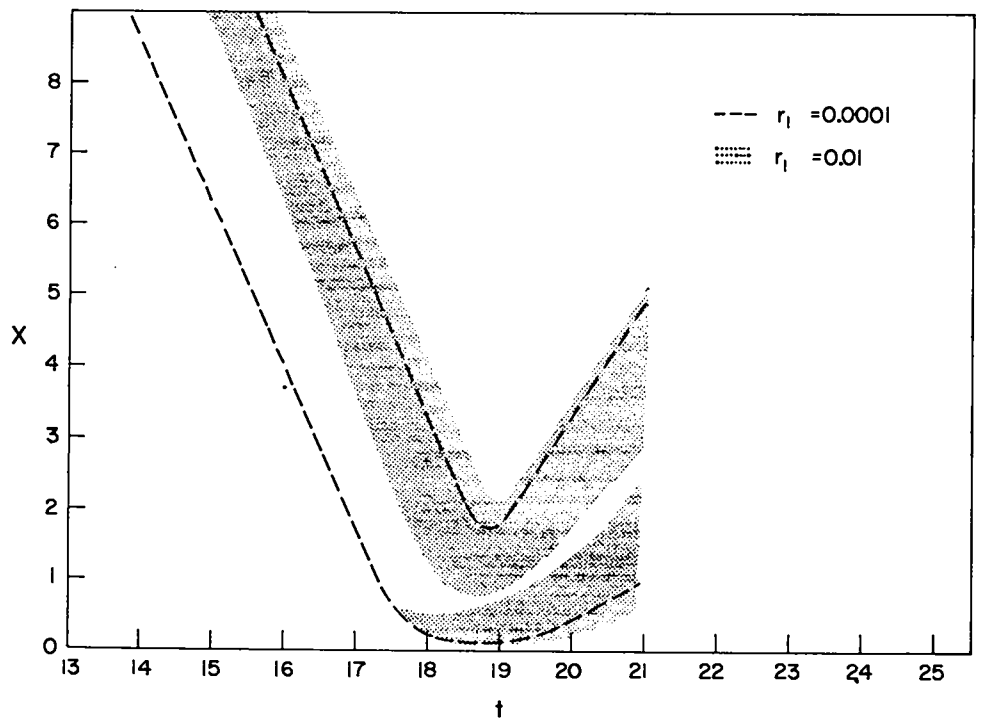

Fig. 13. World lines of Fig. 12 on an expanded scale.

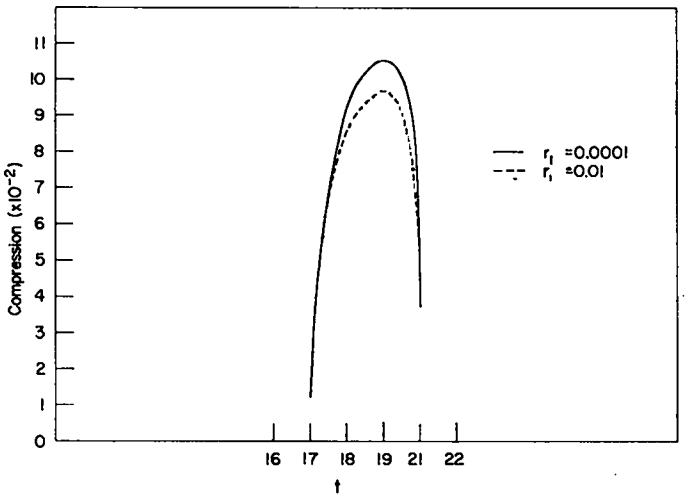

Fig. 14. Average compression of the gas initially in region A.

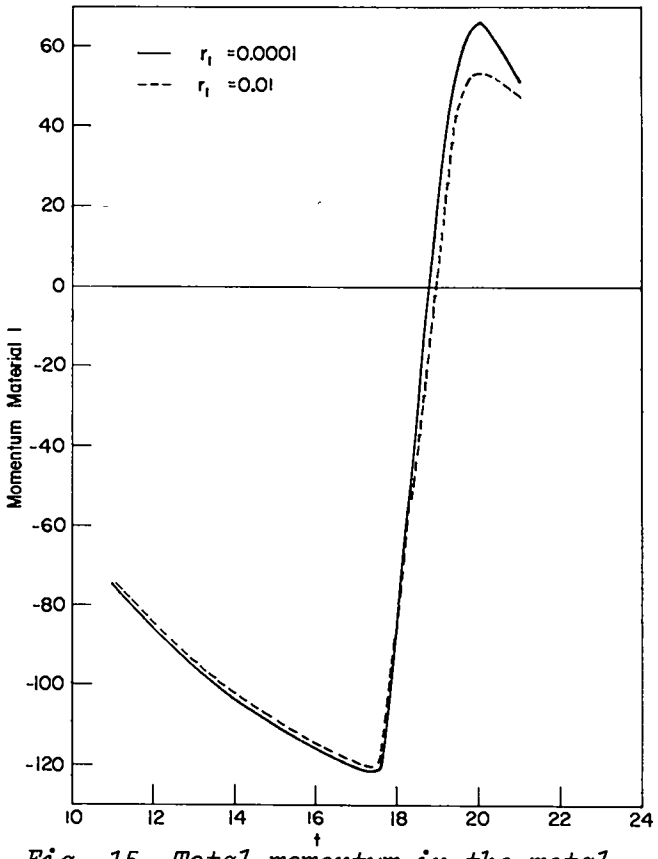

Fig. 15. Total momentum in the metal disc as a function of time.

treatment that examines the direction of acceleration in the region of a computational cell for which this anomalous behavior can be expected. If the acceleration is from the heavy to light material, we expect no interpenetration, and the lighter material is assigned the same fluid velocity as the heavier material. If the acceleration is from the light to heavy material, we expect interpenetration and the code needs no special modification. A test calculation with density ratio 1000 to 1 shows that this modification eliminates the difficulty, and gives results that are similar to those obtained from the 100 to 1 density ratio studies.

VI. CONCLUSIONS

We have performed numerical calculations with a newly modified version of the PIC method by which the relative dynamics of a fragmented metal and a shocked gas can be calculated with both accuracy and efficiency. To test the numerical results, we visualize simple experiments in which a plane shock driven by high explosive through a low-density fluid interacts with a metal composed of various

size fragments. Future comparison with experiments will not only proof-test the methodology, but will also aid in the specification of constitutive relations.

When metal fragments ablate, as they do in some strongly nonequilibrium circumstances, the phase transitions that occur can be inferred from a comparison between calculated and experimental results, enabling us to derive considerable information about the exchange of mass and energy. Such a study would require a calculational model for the phase transition and possible burning that could take place in such an interaction. The phase transition models already developed for the pure Eulerian calculations performed by the KTIF code[4] are likely to be adequate. Both the gas composition and the particle size must be functions of position and time in this modified calculation. If a leap-frog motion of the ablating metal particles produces a local spectrum of particle sizes, or if there is initially such a spectrum in the fragmented metal, an additional modification will be required. This modification can be accomplished with our PIC methodology in the following way.

For every velocity zone we calculate as usual the mean momentum for each material, such that the sum of the particulate momenta equals the calculated total momentum. The individual particles, however, do not have the same velocity for the calculation of their movement through the mesh, each being ascribed a velocity that is an appropriate function of the physical particle size associated with the computational particle. Such a calculation has not yet been performed with the present code. To implement this modification will require a careful examination of the expected velocity spectrum to be associated with a spectrum of particulate sizes. Several models can be visualized, but these must be tested before we can recommend one.

All calculations reported in this study are performed in plane coordinates. We expect a straightforward extension to other geometries. Calculations in three dimensions, however, are as likely for this, as any other technique, to be very expensive in their use of computer time.

APPENDIX A

NUMERICAL ACCURACY

Previous calculations of multiphase flow have been carried out in a completely Eulerian coordinate system. For many purposes this type of representation is sufficiently accurate. In the present circumstances, however, there is one particular feature of the multiphase flow for which our preliminary calculations with a purely Eulerian representation are seriously deficient. Whereas most multiphase flow studies have emphasized the bulk interaction between already mixed phases, our present concern has been with the earliest stages of mix between phases in the vicinity of an interface that is initially sharp. The density plots of Fig. A-1 show that a purely Eulerian calculation performed with a code called MUFF suffers from an intolerable level of numerical diffusion, even with very strong coupling between the two materials. It is easy to show that the diffusion extends over an effective distance that varies as the square root of the size of a computational cell. To reduce the diffusion to an acceptable level, however, would require cells very much smaller than those necessary for accurate resolution of the rest of the dynamics. The realization of this difficulty, confirmed by the numerical calculation shown in Fig. A-1, led to our developing the modified PIC code described in this report. Figure A-2 illustrates that the combined Eulerian and Lagrangian representation of the PIC approach is indeed capable of maintaining a very sharp interface when the coupling between the two materials is strong.

Although the accuracy of the calculations is very difficult to demonstrate in general, we have used two tests to indicate whether the results represent reliable solutions of the differential equations. One test is the calculation of a selected problem with three different degrees of resolution. The results shown in Fig. A-2 indicate relatively little difference among the three calculations, although there is increased sharpness of the interfaces with finer resolution. The second test, discussed in this report, is a study of the propagation of weak signals through an initially mixed region. The agreement of the results with one of the rare analytical solutions obtainable for multiphase flow shows the calculations are reliable.

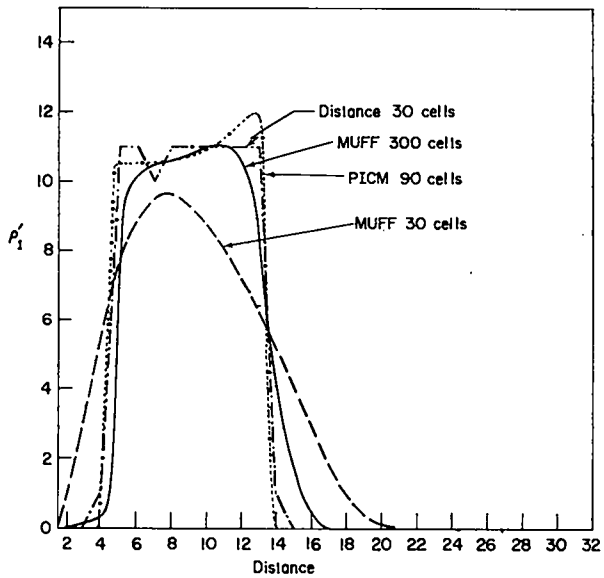

Fig. A-1. A comparison among calculations.

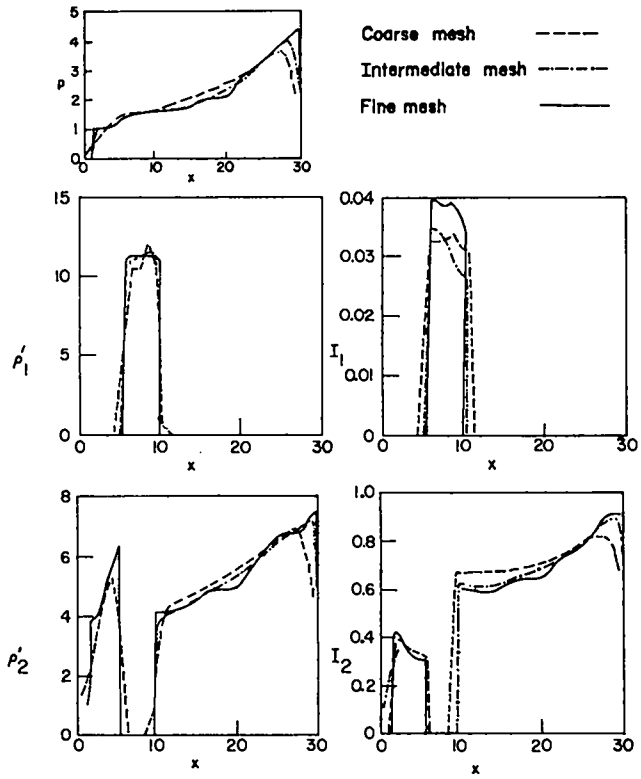

Fig. A-2. PICM calculations with several different resolutions.

APPENDIX B

PICM: AN IMPLICIT VERSION

An alternative implicit version of PICM can be obtained by relating pressure changes to velocity changes and velocity changes to volume changes through a simultaneous time centering of these variables. The resulting equations generally would require solution by iteration. We write the momentum equations in the form

$$ {}^{n}\bar{M}_{1j+\frac{1}{2}} \left({}^{n+1}u_{1j+\frac{1}{2}} - {}^{n}u_{1j+\frac{1}{2}} \right) = {}^{n}\theta_{1j+\frac{1}{2}} \left({}^{n+1}p_{j} - {}^{n+1}p_{j+1} \right) \delta t + {}^{n}K_{j+\frac{1}{2}} \delta x \delta t \left({}^{n+1}u_{2j+\frac{1}{2}} - {}^{n+1}u_{1j+\frac{1}{2}} \right) \qquad \text{(B-1)} $$

and

$$ {}^{n}\bar{M}_{2j+\frac{1}{2}} \left({}^{n+1}u_{2j+\frac{1}{2}} - {}^{n}u_{2j+\frac{1}{2}} \right) = {}^{n}\theta_{2j+\frac{1}{2}} \left({}^{n+1}p_{j} - {}^{n+1}p_{j+1} \right) \delta t + {}^{n}K_{j+\frac{1}{2}} \delta x \delta t \left({}^{n+1}u_{1j+\frac{1}{2}} - {}^{n+1}u_{2j+\frac{1}{2}} \right) , \qquad \text{(B-2)} $$

where the superscript to the left of a variable indicates the time level centering and in the solution procedure becomes the iteration level of that variable. The conservation-of-volume equations are used in the form -

$$ {}^{n+1}D_{1j} \equiv {}^{n+1}V_{1j} - {}^{n}V_{1j} - \left({}^{n+1}u_{1j-\frac{1}{2}} - {}^{n+1}u_{1j+\frac{1}{2}} \right) \delta t = 0 \qquad \text{(B-3)} $$

and

$$ {}^{n+1}D_{2j} \equiv {}^{n+1}V_{2j} - {}^{n}V_{2j} - \left({}^{n+1}u_{2j-\frac{1}{2}} - {}^{n+1}u_{2j+\frac{1}{2}} \right) \delta t = 0 \quad . \qquad \text{(B-4)} $$

At this point we have four equations in five unknowns, ${}^{n+1}V_{1j}$, ${}^{n+1}V_{2j}$, ${}^{n+1}u_{1j+\frac{1}{2}}$, ${}^{n+1}u_{2j+\frac{1}{2}}$, and ${}^{n+1}p_j$. The two equations of state, the conservation of volume fraction, and the assumption of local pressure equilibrium provide us with three more equations and only two additional unknowns, ${}^{n+1}\theta_{1j}$ and ${}^{n+1}\theta_{2j}$.

$$ {}^{n+1}p_j = a_1^2 \left(\frac{{}^{n}M_{1j}}{{}^{n+1}V_{1j}} \frac{1}{{}^{n+1}\theta_{1j}} - \rho_{01} \right) - (\gamma_1 - 1) \frac{{}^{n}M_{1j}}{{}^{n+1}V_{1j}} \frac{1}{{}^{n+1}\theta_{1j}} {}^{n}I_{1j} \quad , \qquad \text{(B-5)} $$

$$ {}^{n+1}p_j = (\gamma_2 - 1) \frac{{}^{n}M_{2j}}{{}^{n+1}V_{2j}} \frac{1}{{}^{n+1}\theta_{2j}} {}^{n}I_{2j} \quad , \qquad \text{(B-6)} $$

and

$$ {}^{n+1}\theta_{1j} + {}^{n+1}\theta_{2j} = 1 \quad . \qquad \text{(B-7)} $$

An additional degree of implicitness could be incorporated in this formulation by expressing the equation of state in terms of advanced-time specific internal energies and by calculating the changes in internal energy by advanced-time work terms. This additional complication will be useful for enhancing the stability of the equations, but is not necessary for the calculation of the low-speed flows for which the above implicitness is proposed.

Proceeding with the system of seven equations presented above, we solve for the iteration variables ${}^{n+1}\theta_{1j}$ and ${}^{n+1}p_j$. We approximate the derivatives of Eqs. (B-3) and (B-4),

$$ {}^{n+1}D_{1j} - {}^{n}D_{1j} = \frac{\partial {}^{n}D_{1j}}{\partial {}^{n}p_j} dp_j + \frac{\partial {}^{n}D_{1j}}{\partial {}^{n}\theta_{1j}} d\theta_{1j} \quad , \tag{B-8} $$

$$ {}^{N+1}D_{2j} - {}^{n}D_{2j} = \frac{\partial {}^{n}D_{2j}}{\partial {}^{n}p_j} dp_j + \frac{\partial {}^{n}D_{2j}}{\partial {}^{n}\theta_{1j}} d\theta_{1j} \quad , \tag{B-9} $$

where dp and dθ represent the changes in those variables from one iteration to the next. Setting ${}^{n+1}D_{1j} = {}^{n+1}D_{2j} = 0$, we obtain

$$ dp_j = \left({}^{n}D_{2j} \frac{\partial {}^{n}D_{1j}}{\partial {}^{n}\theta_{1j}} - {}^{n}D_{1j} \frac{\partial {}^{n}D_{2j}}{\partial {}^{n}\theta_{1j}} \right) \Bigg/ \left(\frac{\partial {}^{n}D_{1j}}{\partial {}^{n}p_j} \frac{\partial {}^{n}D_{2j}}{\partial {}^{n}\theta_{1j}} - \frac{\partial {}^{n}D_{1j}}{\partial {}^{n}\theta_{1j}} \frac{\partial {}^{n}D_{2j}}{\partial {}^{n}p_j} \right) \tag{B-10} $$

and

$$ d\theta_{1j} = \left({}^{n}D_{2j} \frac{\partial {}^{n}D_{1j}}{\partial {}^{n}p_j} - {}^{n}D_{1j} \frac{\partial {}^{n}D_{2j}}{\partial {}^{n}p_j} \right) \Bigg/ \left(\frac{\partial {}^{n}D_{1j}}{\partial {}^{n}p_j} \frac{\partial {}^{n}D_{2j}}{\partial {}^{n}\theta_{1j}} - \frac{\partial {}^{n}D_{1j}}{\partial {}^{n}\theta_{1j}} \frac{\partial {}^{n}D_{2j}}{\partial {}^{n}p_j} \right) \quad . \tag{B-11} $$

The partial derivatives can be evaluated either numerically or analytically. The analytical expressions are complicated and may require the calculation of small differences.

REFERENCES

1. Francis H. Harlow and Anthony A. Amsden, "Numerical Calculation of Multiphase Fluid Flow," J. Comput. Phys. 17, 19-52 (1975).
2. Anthony A. Amsden, "The Particle-in-Cell Method for the Calculation of the Dynamics of Compressible Fluids," Los Alamos Scientific Laboratory report LA-3466 (February 1966).
3. Francis H. Harlow and Anthony A. Amsden, "Flow of Interpenetrating Material Phases," J. Comput. Phys. 18, 440-464 (1975).
4. A. A. Amsden and F. H. Harlow, "K-TIF: A Two-Fluid Computer Program for Downcomer Flow Dynamics," Los Alamos Scientific Laboratory report LA-6994 (January 1978).
5. Francis H. Harlow and Anthony A. Amsden, "Fluid Dynamics," Los Alamos Scientific Laboratory report LA-4700 (June 1971).
6. A. B. Wood, A Textbook of Sound (G. Bell and Sons LTD, London, 1960).
7. Francis H. Harlow, "Two-Dimensional Hydrodynamic Calculations," Los Alamos Scientific Laboratory report LA-2301 (April 1959).

☆U.S. Government Printing Office: 1979 – 677-013/39

Printed in the United States of America. Available from
National Technical Information Service
US Department of Commerce
5285 Port Royal Road
Springfield, VA 22161

Microfiche $3.00

001-025	4.00	126-150	7.25	251-275	10.75	376-400	13.00	501-525	15.25
026-050	4.50	151-175	8.00	276-300	11.00	401-425	13.25	526-550	15.50
051-075	5.25	176-200	9.00	301-325	11.75	426-450	14.00	551-575	16.25
076-100	6.00	201-225	9.25	326-350	12.00	451-475	14.50	576-600	16.50
101-125	6.50	226-250	9.50	351-375	12.50	476-500	15.00	601-up	

Note: Add $2.50 for each additional 100-page increment from 601 pages up.